Plasmonics (2016) 11:865–874
DOI 10.1007/s11468-015-0120-2

Application of Generalized Mie Theory to EELS Calculations as a Tool for Optimization of Plasmonic Structures

Stefan Thomas[1] · Christian Matyssek[2] · Wolfram Hergert[3] · Martin Arnold[4] · Lars Kiewidt[5] · Mirza Karamehmedović[6] · Thomas Wriedt[7]

Received: 19 May 2015 / Accepted: 7 October 2015 / Published online: 2 November 2015

Abstract Technical applications of plasmonic nanostructures require a careful structural optimization with respect to the desired functionality. The success of such optimizations strongly depends on the applied method. We extend the generalized multiparticle Mie (GMM) computational electromagnetic method and use it to excite a system of plasmonic nanoparticles with an electron beam. This method is applied to EELS calculations of a gold dimer and compared to other methods. It is demonstrated that the GMM method is so efficient, that it can be used in the context of structural optimization by the application of genetic algorithms combined with a simplex algorithm. The scheme is applied to the design of plasmonic filters.

✉ Stefan Thomas
sthomas@mpi-halle.mpg.de

[1] Max Planck Institute of Microstructure Physics, Weinberg 2, 06120 Halle, Germany

[2] Institute of Physics, Humboldt University of Berlin, Newton-Straße 15, 12489 Berlin, Germany

[3] Institute of Physics, Martin Luther University, Von-Seckendorff-Platz 1, 06120 Halle, Germany

[4] Institute of Mathematics, Martin Luther University, Theodor-Lieser-Straße 5, 06120 Halle, Germany

[5] Verfahrenstechnik der Wertstoffrückgewinnung, University of Bremen, Post box 330440, 28344 Bremen, Germany

[6] Institut for Fysik, Danmarks Tekniske Universitet, Fysikvej, Building 311, 2800 Kgs. Lyngby, Denmark

[7] IWT, Stiftung Institut für Werkstofftechnik, Badgasteiner Str. 3, 28359 Bremen, Germany

Keywords Mie theory · Optimization · Electron energy loss spectroscopy

Introduction

Electron energy loss spectroscopy (EELS) in the low loss region and cathodoluminescence spectroscopy (CLS) have evolved to common tools to investigate electromagnetic excitations of metallic nanoparticles [1–3]. Especially scattering properties of plasmonic nanostructures like Yagi-Uda antennas [2], plasmonic ridge nanoantennas [4], or plasmonic resonators [5] have been investigated.

Both EELS and CLS experiments are typically performed in transmission electron microscopy (TEM). EELS uses electrons, which are accelerated to 50–300 keV while CLS uses energies of 1–30 keV. In the low loss region, i.e., in the UV-VIS-IR region, we are concerned with the interaction of the electron's electromagnetic field with the sample (typically metallic nanoparticles and systems thereof). The electron interacts with the field scattered back from the sample, which causes characteristic energy losses yielding information on the electromagnetic near field. CLS directly measures the resulting far field scattering patterns. Considering plasmonic particles as nanoantennas, the question of the optimal shape of an antenna for a given purpose arises. Clearly, such an optimization will require computational approaches. We can distinguish semi-analytical approaches mainly based on Mie theory [6] or numerical methods based on the discretization of Maxwell's equations [7].

The original Mie theory describes the scattering of electromagnetic fields at a sphere in terms of an expansion in spherical vector wave functions (SVWF, see Appendix). Since most structures are more complex than a single sphere, more sophisticated methods are needed.

A first generalization of Mie theory was described by Waterman [8] as T-matrix method. The T-matrix contains all interaction contributions, i.e., the interaction of the incident and scattered fields. The T-matrix is calculated from integrals on the surface of the scattering particle. The description of scattering processes at multiple particles can be achieved with the help of rotation and translation addition theorems [9] to create a T-matrix describing the scattering system as a whole including all multiple scattering events [10]. An additional approach, which is used in the present paper, describes the multiple scattering in terms of a system of equations, which relates the coefficients of incident and scattered fields of each particle [11, 12].

Besides these Mie-type codes, the particles can be described as a grid of discrete dipoles (discrete dipole approximation (DDA) [13]), by field expansion using multipoles (generalized multipole technique (GMT) [14]), by the boundary element method (BEM [15]), or by finite element methods like the Discontinuous Galerkin Time Domain method (DGTD [16, 17]).

This wide range of available methods opens up the possibility for optimizations of plasmonic nanostructures with respect to almost any property of interest. Such an optimization will require an efficient method for solving Maxwell's equations and should be flexible with respect to the geometry of the plasmonic system.

The finite element methods offer high flexibility as the spatial discretization allows for an accurate approximation of even complicated structures. Considering efficiency, however, the BEM requires the solution of a dense system of linear equations for each frequency, the DGTD requires the time propagation of the electromagnetic fields until all induced fields have decayed. This results in rather high computational costs for the characterization of a single plasmonic structure. The same holds true for the DDA, which is in principle flexible regarding the geometry of the system, however, a huge number of dipoles have to be used in order to give accurate results, especially in the context of EELS [18].

The T-matrix method is very efficient due to its semi-analytical approach and can handle a variety of different particle geometries [9], covering most of the shapes typically encountered in experiments. A drawback of the method is, however, that in the context of EELS experiments the trajectory of the exciting electron has to lie outside the smallest sphere circumscribing the scatterer. If the scatterer consists of a system of particles, this is obviously a serious restriction.

Several investigations can be found in literature, comparing the advantages and disadvantages of the different methods (cf. [19, 20]).

Plasmonic nanostructures are already a primary target for optimization calculations like optimization of structures with desired resonance spectra by modification of the particle shapes [21], structures for coherent control of light propagation by variation of particle positions and source [22–24], or enhancement of the local electric field by variation of particle positions and sizes [25]. While the first optimization was carried out by evolving a structure towards the desired solution, the latter calculations applied genetic algorithms. The optimization of plasmonic nanostructures in terms of GMM with genetic algorithms was already applied to plane wave excitations [25]. We extend this to an electron beam excitation. Optimization strategies with electron beam excitation are, to the best of our knowledge, not investigated up to now.

If the electron beam excitation is implemented in the generalized multiparticle Mie solution [11, 12], the restriction on the electron's trajectory can be overcome and allows for an optimization of plasmonic structures under electron excitation.

After discussing the theory, the implementation of electron excitation in the GMM method is tested against the T-matrix method and DGTD. The full power of the method in combination with optimization strategies is then demonstrated by means of the design of plasmonic filters.

Theory

Generalized Multiparticle Mie-Solution

The description of scattering by a cluster of spheres starts from Mie theory [6] for a single metallic sphere. Thus, the incident field $\mathbf{E}_{\text{inc}}$, the internal field $\mathbf{E}_{\text{int}}$, and the scattered field $\mathbf{E}_{\text{sca}}$ are expanded in spherical vector wave functions (SVWF) $\mathbf{M}_{mn}^{(1,3)}$ and $\mathbf{N}_{mn}^{(1,3)}$.

$$\mathbf{E}_{\text{inc}} = \sum_{n=1}^{\infty}\sum_{m=-n}^{n} a_{mn}\mathbf{M}_{mn}^{(1)} + b_{mn}\mathbf{N}_{mn}^{(1)} \tag{1a}$$

$$\mathbf{E}_{\text{int}} = \sum_{n=1}^{\infty}\sum_{m=-n}^{n} c_{mn}\mathbf{M}_{mn}^{(1)} + d_{mn}\mathbf{N}_{mn}^{(1)} \tag{1b}$$

$$\mathbf{E}_{\text{sca}} = \sum_{n=1}^{\infty}\sum_{m=-n}^{n} f_{mn}\mathbf{M}_{mn}^{(3)} + g_{mn}\mathbf{N}_{mn}^{(3)} \tag{1c}$$

The boundary condition at the surface (with normal vector $\mathbf{n}$) of the sphere

$$(\mathbf{E}_{\text{inc}} + \mathbf{E}_{\text{sca}} - \mathbf{E}_{\text{int}}) \times \mathbf{n} = 0 \tag{2}$$

yields the well-known Mie coefficients,

$$T_n^1 = -\frac{(m_{\text{r}}L_n(m_{\text{r}}x)+n/x)\,j_n(x)-j_{n-1}(x)}{(m_{\text{r}}L_n(m_{\text{r}}x)+n/x)\,h_n^{(1)}(x)-h_{n-1}^{(1)}(x)} \tag{3a}$$

$$T_n^2 = -\frac{(L_n(m_{\text{r}}x)/m_{\text{r}}+n/x)\,j_n(x)-j_{n-1}(x)}{(L_n(m_{\text{r}}x)/m_{\text{r}}+n/x)\,h_n^{(1)}(x)-h_{n-1}^{(1)}(x)} \tag{3b}$$

which describe the relation between the coefficients of the incident and scattered field in dependence of the relative refractive index $m_\mathrm{r} = \sqrt{\varepsilon_\mathrm{i}/\varepsilon_\mathrm{s}}$, with relative permittivities ε_i and ε_s in the sphere and its surrounding, respectively. The dimensionless size parameter $x = k\,R$ is the product of the wave number and the radius of the sphere. The functions $j_n(x)$ and $h_n^{(1)}(x)$ are spherical Bessel and Hankel functions, respectively. The logarithmic derivative L_n is defined as:

$$L_n(\tilde{x}) = \frac{\mathrm{d}}{\mathrm{d}\tilde{x}}\left[\ln(\tilde{x}\,j_n(\tilde{x}))\right]\,. \tag{4}$$

Using the Mie coefficients, the relation of the expansion coefficients of the incident field $\mathbf{E}_\mathrm{inc}$ and the scattered field $\mathbf{E}_\mathrm{sca}$

$$f_{mn} = T_n^1 a_{mn} \qquad\qquad g_{mn} = T_n^2 b_{mn} \tag{5}$$

can be rewritten in matrix form

$$\begin{pmatrix}\mathbf{f}\\ \mathbf{g}\end{pmatrix} = \underline{\mathbf{T}}\begin{pmatrix}\mathbf{a}\\ \mathbf{b}\end{pmatrix} = \begin{pmatrix}\underline{\mathbf{T}}^1 & 0\\ 0 & \underline{\mathbf{T}}^2\end{pmatrix}\begin{pmatrix}\mathbf{a}\\ \mathbf{b}\end{pmatrix} \tag{6}$$

where $\underline{\mathbf{T}}$ defines the scattering matrix (T-matrix) for a single spherical particle [26]. The multiple scattering of N spheres can be described by means of a system of equations, which relates the coefficients of the scattered waves of all involved spheres using the SVWF's translation coefficients $A_{mn}^{\mu\nu}(j,i)$ and $B_{mn}^{\mu\nu}(j,i)$. The translation coefficients transform the scattered waves from particle j with indices μ,ν into incident waves on particle i with expansion coefficients m,n, i.e., the coefficients depend on the relative separation and direction of the particles.

$$f_{mn}^i = T_{i,n}^1 \times \left(a_{mn}^i - \sum_{\substack{j=1\\ i\neq j}}^{N}\sum_{\nu=1}^{\infty}\sum_{\mu=-\nu}^{\nu}\left(f_{\mu\nu}^j A_{mn}^{\mu\nu}(j,i) + g_{\mu\nu}^j B_{mn}^{\mu\nu}(j,i)\right)\right) \tag{7a}$$

$$g_{mn}^i = T_{i,n}^2 \times \left(a_{mn}^i - \sum_{\substack{j=1\\ i\neq j}}^{N}\sum_{\nu=1}^{\infty}\sum_{\mu=-\nu}^{\nu}\left(f_{\mu\nu}^j B_{mn}^{\mu\nu}(j,i) + g_{\mu\nu}^j A_{mn}^{\mu\nu}(j,i)\right)\right) \tag{7b}$$

If Eqs. 7a and 7b are recasted in matrix form, standard solvers for linear systems of equations can be easily applied.

$$\left[\begin{pmatrix}\underline{\mathbf{I}} & 0\\ 0 & \underline{\mathbf{I}}\end{pmatrix} + \begin{pmatrix}\underline{\mathbf{T}}^1 & 0\\ 0 & \underline{\mathbf{T}}^2\end{pmatrix}\begin{pmatrix}\underline{\mathbf{A}} & \underline{\mathbf{B}}\\ \underline{\mathbf{B}} & \underline{\mathbf{A}}\end{pmatrix}\right]\begin{pmatrix}\mathbf{f}\\ \mathbf{g}\end{pmatrix} = \begin{pmatrix}\underline{\mathbf{T}}^1 & 0\\ 0 & \underline{\mathbf{T}}^2\end{pmatrix}\begin{pmatrix}\mathbf{a}\\ \mathbf{b}\end{pmatrix} = \begin{pmatrix}\tilde{\mathbf{a}}\\ \tilde{\mathbf{b}}\end{pmatrix} \tag{8}$$

To calculate the matrices $\underline{\mathbf{A}}$ and $\underline{\mathbf{B}}$ containing the translation coefficients $A_{mn}^{\mu\nu}(j,i)$ and $B_{mn}^{\mu\nu}(j,i)$, Mackowski's three-step-method [27] is used,

$$\underline{\mathbf{A}}_{ij}(\mathbf{r}_{ij}) = \underline{\mathbf{R}}^{-1}(\mathbf{r}_{ij})\tilde{\underline{\mathbf{A}}}_{ij}(r_{ij})\underline{\mathbf{R}}(\mathbf{r}_{ij}) \tag{9a}$$

$$\underline{\mathbf{B}}_{ij}(\mathbf{r}_{ij}) = \underline{\mathbf{R}}^{-1}(\mathbf{r}_{ij})\tilde{\underline{\mathbf{B}}}_{ij}(r_{ij})\underline{\mathbf{R}}(\mathbf{r}_{ij}) \tag{9b}$$

where the matrices $\tilde{\underline{\mathbf{A}}}_{ij}$ and $\tilde{\underline{\mathbf{B}}}_{ij}$ describe the axial translation, and the unitary matrix $\underline{\mathbf{R}}$ describes the rotation of the coordinate system.

As a result, the calculation yields the expansion coefficients f_{mn}^i and g_{mn}^i of the scattered field at each individual particle due to the multiple scattering in the particle system. In contrast to the GMM method, the T-matrix method provides one set of expansion coefficients for the whole scattering system.

Excitation

To perform calculations with the GMM method, it is necessary to expand the incident field in SVWFs. The expansion coefficients for an incident plane wave [28] and an incident electron beam [29] are in principle known, but due to varying definitions of the SVWFs, used in literature, the coefficients are presented here with respect to the definition of the SVWFs given by Doicu et al. [9] (cf. Appendix).

In general, the expansion (1a) can be calculated by integration of the incident field $\mathbf{E}_\mathrm{inc}$ over an auxiliary sphere, because the SVWFs form a complete set of orthogonal basis functions on the unit sphere.

$$a_{mn} = \frac{\int_0^\pi \mathrm{d}\theta\int_0^{2\pi}\mathrm{d}\varphi\mathbf{E}_\mathrm{inc}\mathbf{M}_{mn}^{(1)}\sin\theta}{\int_0^\pi \mathrm{d}\theta\int_0^{2\pi}\mathrm{d}\varphi|\mathbf{M}_{mn}^{(1)}|^2\sin\theta} \tag{10a}$$

$$b_{mn} = \frac{\int_0^\pi \mathrm{d}\theta\int_0^{2\pi}\mathrm{d}\varphi\mathbf{E}_\mathrm{inc}\mathbf{N}_{mn}^{(1)}\sin\theta}{\int_0^\pi \mathrm{d}\theta\int_0^{2\pi}\mathrm{d}\varphi|\mathbf{N}_{mn}^{(1)}|^2\sin\theta} \tag{10b}$$

For a given incident field $\mathbf{E}_\mathrm{inc}$, we are thus able to determine the corresponding expansion coefficients. In case of an incident plane wave, the following non-vanishing coefficients

$$a_{1,n} = -a_{-1,n} = \mathrm{i}^{n-1}\sqrt{2n+1} \tag{11}$$

$$b_{1,n} = b_{-1,n} = \mathrm{i}^{n-1}\sqrt{2n+1} \tag{12}$$

describe the excitation.

To calculate the expansion coefficients of an electron beam excitation, we restrict the problem to an electron flying in z-direction with velocity v while using reduced units, in particular the speed of light in vacuum is $c_0 = 1$. The problem is considered in frequency domain, i.e., the coefficients do not depend on time t but on the frequency ω. The position of the electron relative to the center of the sphere is then given in cylindrical coordinates $\mathbf{r}_0 = (b,\varphi_0,z_0)$ (see Fig. 1). The distance b of the electron from the z axis is commonly known as impact parameter. The derivation

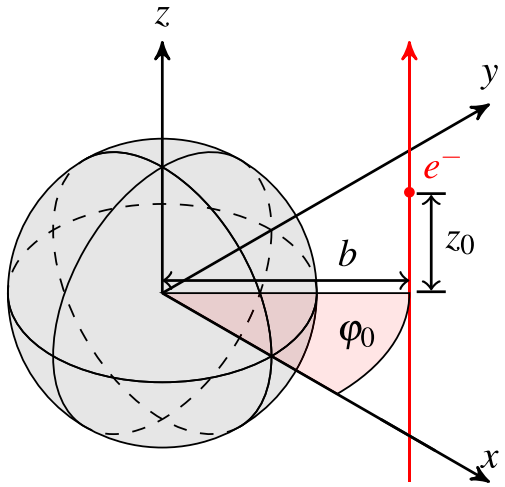

Fig. 1 Excitation of a sphere by the field by an electron beam. The actual position of the electron in cylindrical coordinates is $\mathbf{r}_0 = (b, \varphi_0, z_0)$

[30] shows that the impact parameter has a monotonic influence on the magnitude of the expansion coefficients, i.e., the larger the impact parameter, the smaller the magnitude of the expansion coefficients. The azimuthal angle φ_0 and height position z_0 solely result in a complex phase, and thus, the influence of the electron's position $\mathbf{r}_0$ is summarized in the factor R_m.

$$R_m = K_m\left(\frac{\omega b}{v}\frac{1}{\gamma}\right)\exp\left(-\mathrm{i}m\varphi_0 - \mathrm{i}\frac{\omega b}{v}\frac{z_0}{b}\right) \tag{13}$$

$$a_{mn} = R_m \frac{\mathrm{i}^{n-2m}k}{\pi}\left(\frac{2}{n(n+1)}\right)^{\frac{1}{2}} m\, P_n^{|m|}(v^{-1}) \tag{14}$$

$$\begin{aligned} b_{mn} = {} & R_m \frac{\mathrm{i}^{n-2m}k}{\pi}\left(\frac{2}{n(n+1)}\right)^{\frac{1}{2}} \frac{i}{2v\gamma} \\ & \times \left(c_{m-1}^{+}\sqrt{(n-m+1)(n+m)}P_n^{|m-1|}(v^{-1})\right. \\ & \left. -c_{m-1}^{-}\sqrt{(n+m+1)(n-m)}P_n^{|m+1|}(v^{-1})\right) \end{aligned} \tag{15}$$

The functions $P_n^{|m|}$ are associated Legendre polynomials, and the K_m are modified Bessel functions of the second kind. The Lorentz factor is given by $\gamma^{-1} = \sqrt{1-v^2}$ in our units and the factors $c_m^{+/-}$ take care of the correct signs due to the usage of $|m|$ in the associated Legendre polynomials.

$$c_m^{+} = \begin{cases} 1 & m < 0 \\ -1 & m \geq 0 \end{cases} \qquad c_m^{-} = \begin{cases} 1 & m \leq 0 \\ -1 & m > 0 \end{cases} \tag{16}$$

Electron Energy Loss Spectroscopy and Cathodoluminescence Spectroscopy

The numerical calculation of EELS and CLS differs, because the scattered field $\mathbf{E}_{\mathrm{sca}}$ enters the signals in a different way.

The electron energy loss is the result of the force, the electron with velocity $\mathbf{v}_e(t)$ experiences along its path $\mathbf{r}_e(t)$, due to the interaction with the scattered field $\mathbf{E}_{\mathrm{sca}}$

$$\Delta E = e\int_{-\infty}^{\infty} \mathrm{d}t\, \mathbf{v}_e(t)\cdot\mathbf{E}_{\mathrm{sca}}(\mathbf{r}_e(t), t)\,. \tag{17}$$

The electron energy loss can be expressed also in terms of an integral over the frequency dependent electron energy loss probability $P(\omega)$

$$\Delta E = \hbar\int_{0}^{\infty} \mathrm{d}\omega\, \omega P(\omega)\,. \tag{18}$$

Using the Fourier representation of the scattered field $\mathbf{E}_{\mathrm{sca}}$ and the assumption that the momentum of the electron remains constant (no-recoil approximation, NRA), Eq. 17 can be reformulated as an integral in frequency domain similar to Eq. 18. By comparison of both expressions, the electron energy loss probability can be calculated (cf. [17]) from

$$P_{\mathrm{EELS}}(\omega) = \frac{2e}{\hbar\omega}\int_{-\infty}^{\infty} \mathrm{d}t\, \Re\left\{\mathbf{v}_e(t)\cdot\mathbf{E}_{\mathrm{sca}}(\mathbf{r}_e(t),\omega)\mathrm{e}^{-\mathrm{i}\omega t}\right\}\,. \tag{19}$$

Due to a further application of the NRA, i.e., by substituting $\mathbf{r}_e(t) = \mathbf{r}_0 + \mathbf{v}t$, Eq. 19 becomes suitable for frequency domain calculations. Assuming that the electron moves only in z-direction, we find the following alternative definition:

$$P_{\mathrm{EELS}}(\omega) = \frac{2e}{\hbar\omega}\int_{-\infty}^{\infty} \mathrm{d}z\, \Re\left\{\mathbf{e}_z\cdot\mathbf{E}_{\mathrm{sca}}(\mathbf{r}_0,\omega)\mathrm{e}^{-\mathrm{i}\omega z/v}\right\}\,. \tag{20}$$

The cathodoluminescence probability is given by the amount of scattered energy and thus can be calculated by integrating the Poynting vector over a closed surface circumscribing the scatterer. For the sake of simplicity, this surface should be a sphere.

$$\Delta E = \int_0^{\pi}\mathrm{d}\theta\int_0^{2\pi}\mathrm{d}\varphi\int_{-\infty}^{\infty}\mathrm{d}t\, r^2\mathbf{e}_r\cdot(\mathbf{E}\times\mathbf{H}) \tag{21}$$

Again, this energy loss can be expressed in terms of a loss probability in frequency domain.

$$\Delta E = \int_0^{\pi}\mathrm{d}\theta\int_0^{2\pi}\mathrm{d}\varphi\int_{0}^{\infty}\mathrm{d}\omega\,\omega\, P_{\mathrm{CL}}(\omega,\theta,\varphi) \tag{22}$$

Thus, the Fourier transform of Eq. 21 compared with Eq. 22 provides an expression for the angular-dependent cathodoluminescence probability

$$P_{\mathrm{CL}}(\omega,\theta,\varphi) = \frac{r^2}{\omega}\Re\left\{[\mathbf{E}(\omega,\theta,\varphi)\times\mathbf{H}(\omega,\theta,\varphi)]\cdot\mathbf{e}_r\right\}\,. \tag{23}$$

The far field expressions of the fields can be used, if the radius of the circumscribing sphere goes to infinity. This

removes the magnetic field from the calculation. Finally, the cathodoluminescence probability is calculated from

$$P_{\mathrm{CL}}(\omega,\theta,\varphi) = \frac{1}{\omega}\sqrt{\frac{\varepsilon_{\mathrm{S}}}{\mu_{\mathrm{S}}}}\,|\mathbf{E}(\theta,\varphi)|^2 \ . \tag{24}$$

Optimization

A two-step approach was used to achieve optimization of nano-plasmonic structures. First, starting from a set of random configurations of the system of interest, genetic algorithms were used for a large-scale scan of the parameter space and a coarse optimization towards the optimal configuration. In a second step, further optimization was achieved by means of the simplex algorithm of Nelder and Mead [31] to get the best configurations according to the optimization criteria.

The genetic algorithms were developed with natural evolution processes in mind. The basic idea is that a population, consisting of a larger amount of different configurations, evolves over time. To achieve this, the fitness for each individual configuration (also called individuum) gets evaluated. This fitness is usually a measurable quantity like the field strength at a certain position but can be any arbitrary quantity, which should be optimized. The fitness function, used during the optimization of plasmonic filters in this paper, is the ratio of magnitude of the electric field next to a receiver sphere for two different wavelengths.

$$F = \log\left(\frac{|\mathbf{E}_{\lambda_1}|}{|\mathbf{E}_{\lambda_2}|}\right) \tag{25}$$

This definition is inspired by typical near field enhancement optimizations, where the local field is compared to the normalized intensity of the incoming plane wave excitation [25] and optimization of surface structures for surface enhanced raman spectroscopy (SERS) [32]. Possible applications for resulting structures include the frequency filtered, localized excitation of molecules positioned at the measuring point.

After calculating the fitness, the best configurations of the population get used to create the next generation's population by direct copying (elitism), interchange of components of the configurations (crossover), or modification of single quantities in the configurations (mutation). By repeating these steps for several generations, the population converges to good approximants of the optimal structure.

At this point, the simplex algorithm from Nelder and Mead [31] gets used, to optimize the best structures, selected from the previous calculation. The idea of this algorithm is to calculate the fitness of configurations with small deviations from the original configuration, thus spanning a simplex in configuration space, whose vertices are assigned the corresponding fitness. Then, a replacement for the vertex with the worst fitness is calculated in a way that either a better vertex is found or the simplex gets contracted towards the best vertex. Repeating this process, the simplex converges to the local minimum which is likely a global minimum, due to the precedent optimization with genetic algorithms.

However, the search of nearly-optimal structures with genetic algorithms is subject of a quick reduction of parameter space, which requires either a brute-force approach to search in a larger set of parameters or a sophisticated algorithm to preserve/restore the spanned parameter space during the optimization. The latter approach can be achieved by principal component analysis to recover from a population degeneration [33].

In this study, the traditional genetic algorithms were implemented using the GENETIC ALGORITHM UTILITY LIBRARY [34]. To overcome the problem of population degeneration, 100 distinct populations with 20 individuals each have been used during the optimization. Crossover happened in 80 % and mutation in 30 % of all evolution steps. The evolution was calculated over 100 generations. The simplex algorithm was implemented using the GNU SCIENTIFIC LIBRARY [35].

Additionally, the SHUFFLED COMPLEX EVOLUTION WITH PRINCIPAL COMPONENTS ANALYSIS (SP-UCI [33]), which incorporates a modified simplex algorithm and multinormal resampling for avoidance of population degeneration, was used to compare to the other procedure. For this algorithm, 20 distinct populations with 155 species each were used.

Examples and Application

First, a dimer of two gold spheres is used to compare our implementation of EELS and CLS calculation in the GMM method with the results of T-matrix method and DGTD [17, 36]. The combination of the advantages of the generalized multiparticle Mie (GMM) method with the above mentioned optimization strategy leads to a very efficient method to optimize complex plasmonic nanostructures. This will be demonstrated by the design of plasmonic filters.

Dimer of two Gold Spheres

First, we compare the electron energy loss propability $P_{\mathrm{EELS}}(\omega)$ calculated for a dimer of two gold spheres by the GMM method with the results from the T-matrix method and the DGTD. The gold spheres have a radius of 10 nm and a distance of 1 nm, which are typical parameters from actual experiments [37]. The electron passes this dimer at the outer edge with a distance of 0.5 nm at 30 % of the speed of light. Due to the mentioned restrictions of the T-matrix method, the electron beam has to pass the dimer outside of the smallest circumscribing sphere. Although experimental

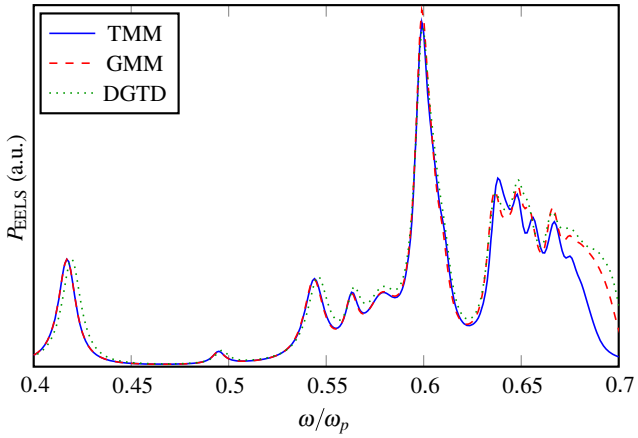

Fig. 2 Comparison of the electron energy loss probability $P_{\mathrm{EELS}}(\omega)$ for a Au dimer, calculated with T-matrix method (TMM), generalized multiparticle Mie (GMM) method, and Discontinuous Galerkin Time Domain method (DGTD)

values for the permittivity can be used in the framework of the T-matrix and GMM methods, the DGTD method is restricted to an analytical description of the permittivity. As the choice of a complex model for the permittivity will heavily influence the computation cost of the DGTD, we chose the Drude model for a free electron gas

$$\varepsilon_{\mathrm{r}}(\omega) = 1 - \frac{\omega_{\mathrm{p}}^2}{\omega(\omega + \mathrm{i}\eta)} \tag{26}$$

to get a reasonably fast calculation. Nevertheless, it is well known that gold is much better described by extending the Drude model with additional Lorentzian terms [38] or critical points describing the interband transitions [39]. The parameters in the Drude model (26) are the plasma frequency ω_{p} ($\hbar\omega_{\mathrm{p}} = 9.073$ eV) and the relaxation rate η ($\hbar\eta = 0.071$ eV) that accounts for the electromagnetic damping. These values were acquired by fitting experimental values [40, 41] and are similar to other previously published parameters [42–44].

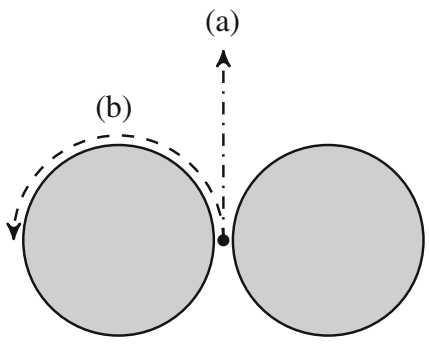

Fig. 3 Variation of the position of the exciting electron beam near the dimer, starting at the center of the dimer. **a** perpendicular to the dimer axis, **b** on a circle around one Au sphere with constant impact parameter

The calculation of light scattering in the (sub-)nanometer regime requires, in general, careful consideration of non-local effects. The implementation of non-local effects could be achieved in terms of the hydrodynamical model as extension to the present Drude model [45]. The influence of non-local effects was already discussed by Abajo [46] theoretically and by Duan et al. [47] in comparison of theory and experiment. Abajo [46] showed that typical effects like blue-shift of the resonances and plasmon broadening appears for gold dimers with a radius of 10 nm for a distance of the spheres much below 1 nm. Therefore, the non-local effects are not taken into account for the comparison of the three methods.

Figure 2 shows the comparison of the three methods. Both the T-matrix method and the generalized multiparticle Mie method were carried out with a maximum multipole order of $n = 16$ to get comparable results. Due to numerical difficulties, the TMM cannot be used to calculate higher multipole orders, while the GMM method is more stable [48].

All curves in the plot are normalized to the height of the first peak. We can clearly see that the results of the TMM and the GMM method show very good agreement for lower frequencies, while there are small differences for frequencies $\omega \geq 0.65\omega_{\mathrm{p}}$. This can be explained by the poorer convergence properties of the TMM. However, with increasing multipole order, the TMM results show a tendency towards the results of the GMM method. The results of the DGTD agree well with the GMM method, but the peaks at lower frequency are slightly shifted to higher frequency and the magnitude of the loss probability differs for

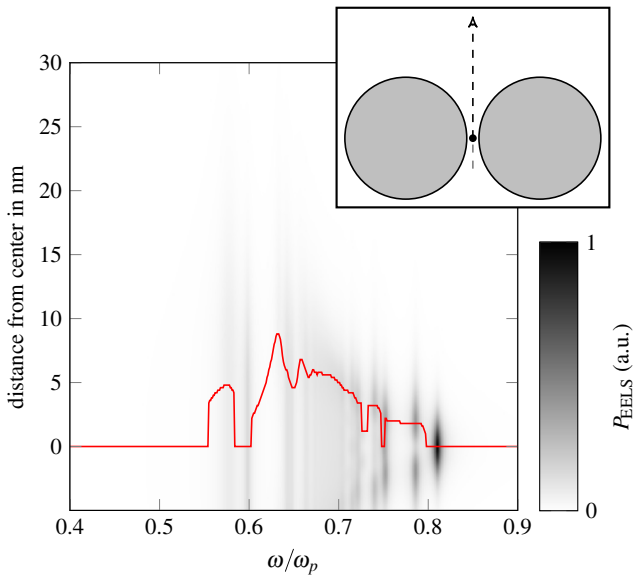

Fig. 4 Electron energy loss probability $P_{\mathrm{EELS}}(\omega)$ for path (**a**) from Figure 3. The *solid red line* marks the distance, at which the highest energy loss probability for a given frequency was detected

the higher frequencies. Again, this could be explained by the missing convergence, because a very fine real space mesh is necessary to describe the interaction between the electron and the gold spheres and the realization of the Fourier transform requires the fields to be mostly decayed, i.e., a long simulation in the time domain.

In contrast to the other methods, the GMM method allows a more detailed and fast investigation of the dimer. We do not have restrictions for the position of the exciting electron beam; therefore, the excitation can be varied along the paths shown in Fig. 3.

At first, we start with the excitation at the center of the dimer and move it away, perpendicularly to the dimer axis (path (a) in Fig. 3). The results of the calculation (cf. Fig. 4) demonstrate that the electron energy loss probability (EELP) for higher frequencies decays faster than for lower frequencies, which is due to the different wavelength, which influences the decay length of the near field. It is also remarkable that the maximum achievable EELP (marked in red in Fig. 4) is not always at the center of the dimer but at a distance of up to 10 nm. A similar study has been carried out moving the electron beam with constant impact parameter of $b = 10.5$ nm on a circle around one of the gold spheres (path (b) in Fig. 3). Along this way, the electron beam can excite certain modes, while other modes cannot be excited due to symmetry reasons (Fig. 5). The modes excited or not are classified usually as optical bright and dark modes, respectively. In dependence on the frequency, the highest loss probability appears at specific angles, as a result of the plasmon mode geometries with different nodal points.

The investigation of optical bright and dark modes can be further extended. Due to their symmetry properties, dark

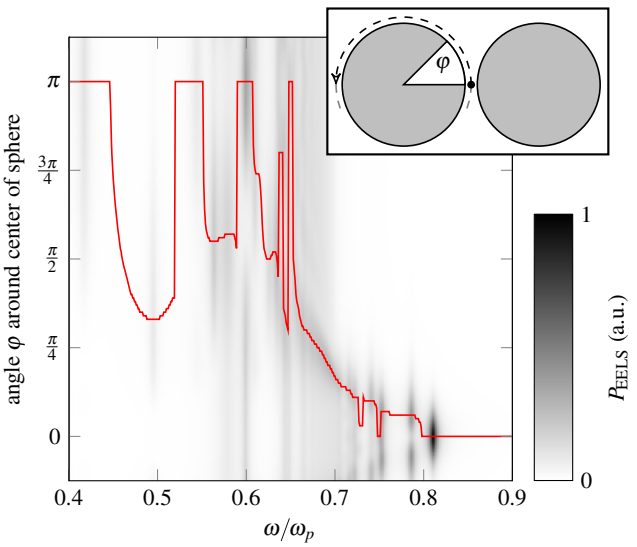

Fig. 5 Electron energy loss probability $P_{\mathrm{EELS}}(\omega)$ for path (**b**) from Fig. 3. The *solid red line* marks the angle, at which the highest energy loss probability for a given frequency was measured

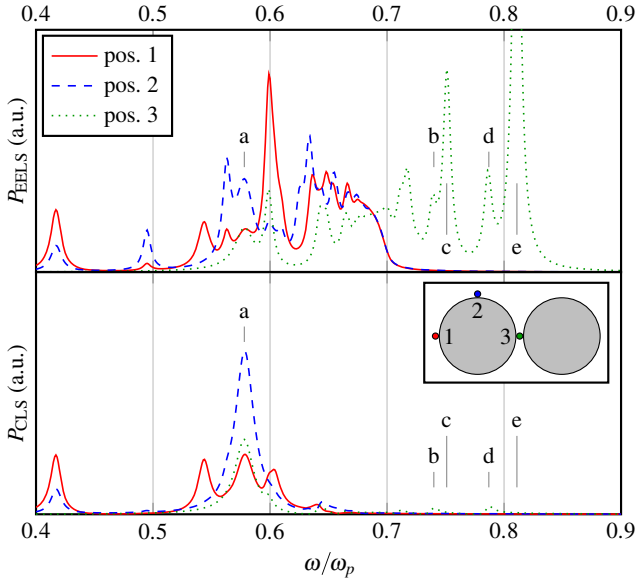

Fig. 6 Electron energy loss probability and cathodoluminescence probability for a gold dimer excited at three different points

modes cannot couple to the far field. Thus, the cathodoluminescence probability (CLP), which is a physical quantity determined from the far field, should be zero for these modes (see Fig. 6). From the symmetry of the structure, we can predict that the excitation by an electron beam, which is directed through the center of the dimer, can excite dark modes oscillating in the x-y-plane. Due to the electron passing the dimer, it is also possible to excite optical bright modes with polarization in z-direction.

By examining the resulting spectra (see Fig. 6), one can see that indeed the excitations at positions 1 and 2 create strong contributions in both EELS and CLS in the lower frequency range, while the excitation in the center of the dimer (position 3) results also in contributions to the EELS in the higher frequency range, while the CLS shows small to none contributions in this frequency range. Thus, the modes c and e can be considered to be dark modes, while there are also two bright modes (b and d) close to them.

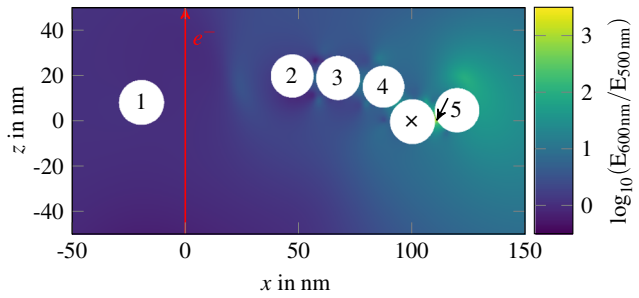

Fig. 7 Contrast between scattered fields for $\lambda = 500$ nm and $\lambda = 600$ nm. The *arrow* points to the point where the field is measured to optimize the system. The *white areas* are the cut of the x–z-plane with the spheres

Table 1 Optimized positions for the plasmonic filter (see Fig. 7)

Sphere	x in nm	y in nm	z in nm
1	−19.5	−0.4	8.4
2	47.0	−2.9	20.1
3	67.2	−2.1	19.2
4	87.2	−3.8	15.4
Fixed sphere	100.0	0.0	0.0
5	119.6	−1.6	5.0

A very interesting contribution to all three spectra is mode a, with a frequency which corresponds to the frequency of the dipole mode of a single sphere which is directed along the electron path. This mode can be excited from all three positions but is most prominent in the cathodoluminescence spectra.

Plasmonic Filter

The strength of the GMM becomes apparent in the optimization of plasmonic nanostructures. While most authors concentrate their work on structures with large near field enhancement [49, 50], necessary for surface enhanced Raman spectroscopy (SERS), it is also interesting to use ensembles of spheres as plasmonic filters. This means that, e.g., a signal of broad frequency range is used to excite the structure, but only a certain frequency range should pass. This is a plasmonic analogue to bandpass filters in acoustics and electronics. The broad band excitation in our case is provided by the electron beam.

The structure considered here consists of a fixed sphere (marked by a cross in Fig. 7) next to the reference point where the field is measured and a fixed electron beam, whose electrons had a velocity of $v = 0.3\ c_0$. Additionally, five spheres were positioned by means of the described optimization procedures to get a high contrast between two wavelengths (we fixed the wavelengths to 500 and 600 nm). The radii of all six spheres were fixed to 10 nm, and the positions were restricted to the volume described by $x, y \in -3030$ nm and $z \in -25125$ nm.

According to Eq. 25, the fitness, i.e., the quality of a structure, was measured to be

$$F = \log\left(\frac{|\mathbf{E}_{600\text{ nm}}|}{|\mathbf{E}_{500\text{ nm}}|}\right). \tag{27}$$

Within the first procedure (i.e. genetic algorithms combined with simplex algorithm), the coarse optimization process for the plasmonic filter yielded various different results indicating a complicated fitness function. From these configurations, the best structures were further optimized using the simplex method and all results showed a similar structure, i.e., they consisted of one sphere next to the electron beam to "catch" the field of the electron and an arc formed by the remaining spheres to guide this field to the measuring point.

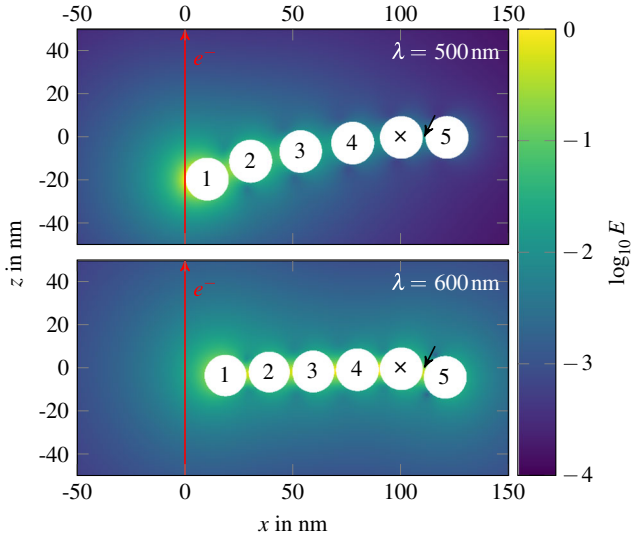

Fig. 8 Optimization of the structure with respect to the field strength at a reference point for a given wavelength

The results obtained from SP-UCI showed similar behavior, though there are no coarse intermediate results available because this algorithm already includes a simplex method for fine optimization. Over the course of this study, the SP-UCI method yielded the better results.

The spheres are mainly positioned in the x-z-plane and show a tendency to be perfectly inplane. However, the fine optimization towards these perfectly optimized structures requires an extreme amount of evaluations to move the spheres in place (Table 1).

As a comparison, we also optimized this structure to get the highest possible field intensity for both wavelengths separately, by defining the fitness as $F = |\mathbf{E}|$. The result (cf. Fig. 8) shows that even though the intensity of the field has its highest peak at 500 nm next to the electron beam, the intensity at the receiving point differs by an order of magnitude between the two wavelengths and is largest for 600 nm. The structures differ strongly for the two wavelengths (Tables 2 and 3).

Table 2 Optimized positions for 500 nm (see Fig. 8)

Sphere	x in nm	y in nm	z in nm
1	10.1	0.0	−19.4
2	30.2	0.0	−11.1
3	53.4	0.0	−6.5
4	77.5	0.0	−2.6
fixed sphere	100.0	0.0	0.0
5	121.1	0.0	0.0

Table 3 Optimized positions for 600 nm (see Fig. 8)

Sphere	x in nm	y in nm	z in nm
1	18.5	2.3	−3.1
2	38.8	2.9	−1.5
3	59.2	1.9	−1.3
4	79.7	0.5	−0.5
fixed sphere	100.0	0.0	0.0
5	120.3	0.3	−4.0

It is important to note that the optimized structures have particle distances down to 0.2 nm. As a result, the scattering processes might be subject to non-local effects and further calculations might be necessary.

Conclusions

The generalized multiparticle Mie (GMM) method, developed in the context of plane wave excitation of particle systems, was extended to electron beam excitations of systems of metallic particles. The accuracy of the method was demonstrated in comparison with the T-matrix method and the DGTD. The power of the combination of the GMM method with advanced optimization strategies was demonstrated by the optimization of plasmonic filter structures. If the shape of the single particle is a sphere, the method can be extended to systems consisting of much more particles.

Appendix

The spherical vector wave functions (SVWF) can be constructed from the spherical wave functions (SWF). The SWFs are scalar solutions to the Helmholtz equation and can be written as

$$u_{mn}^{1,3}(k\,\mathbf{r}) = z_n^{1,3}(k\,r)\,P_n^{|m|}(\cos\theta)\mathrm{e}^{\mathrm{i}m\varphi}\,, \tag{28}$$

with $n = 1, 2, \ldots$, $m = -n, \ldots, n$. (r, θ, ϕ) are the spherical coordinates of the position vector $\mathbf{r}$. Following the definition of [9], the radial part is the spherical Bessel function of first kind $z_n^1(kr) = j_n(kr)$ and the spherical Hankel function of first kind $z_n^3(kr) = h_n^{(1)}(kr)$ for incoming and outgoing waves, respectively. The polar part of the wave function is given by the associated Legendre polynomials, which depends on the magnitude of m.

Finally, the SVWFs can be constructed using the pilot vector $\mathbf{r}$.

$$\mathbf{M}_{mn}^{1,3}(k\,\mathbf{r}) = \frac{1}{\sqrt{2n(n+1)}}\nabla u_{mn}^{1,3}(k\,\mathbf{r})\times\mathbf{r} \tag{29}$$

$$\mathbf{N}_{mn}^{1,3}(k\,\mathbf{r}) = \frac{1}{k}\nabla\times\mathbf{M}_{mn}^{1,3}(k\,\mathbf{r}) \tag{30}$$

The final expressions used in this paper are

$$\mathbf{M}_{mn}^{1,3}(k\,\mathbf{r}) = \frac{z_n^{1,3}(k\,r)}{\sqrt{2n(n+1)}}\left(\mathrm{i}m\pi_n^{|m|}(\theta)\mathbf{e}_\theta - \tau_n^{|m|}(\theta)\mathbf{e}_\varphi\right)\mathrm{e}^{\mathrm{i}m\varphi} \tag{31}$$

$$\mathbf{N}_{mn}^{1,3}(k\,\mathbf{r}) = \frac{1}{\sqrt{2n(n+1)}}\left(n(n+1)\frac{z_n^{1,3}(k\,r)}{k\,r}P_n^{|m|}(\cos\theta)\mathbf{e}_r + \frac{[k\,r z_n^{1,3}(k\,r)]'}{k\,r}\left(\tau_n^{|m|}(\theta)\mathbf{e}_\theta + \mathrm{i}m\pi_n^{|m|}(\theta)\mathbf{e}_\varphi\right)\right)\mathrm{e}^{\mathrm{i}m\varphi} \tag{32}$$

The angular functions τ and π are defined using the associated Legendre polynomials P_n^m as

$$\tau_n^m(\theta) = \frac{\mathrm{d}}{\mathrm{d}\theta}P_n^m(\cos\theta), \qquad \pi_n^m(\theta) = \frac{P_n^m(\cos\theta)}{\sin\theta}\,. \tag{33}$$

References

1. García de Abajo FJ (2010) Rev Mod Phys 82(1):209. doi:10.1103/RevModPhys.82.209
2. Coenen T, Vesseur EJR, Polman A, Koenderink AF (2011) Nano Lett 11(9):3779. doi:10.1021/nl201839g
3. von Cube F, Irsen S, Niegemann J, Matyssek C, Hergert W, Busch K, Linden S (2011) Opt Mater Express 1(5):1009. doi:10.1364/OME.1.001009
4. Coenen T, Vesseur EJR, Polman A (2012) ACS Nano 6(2):1742. doi:10.1021/nn204750d
5. Vesseur EJR, Aizpurua J, Coenen T, Reyes-Coronado A, Batson PE, Polman A (2012) MRS Bulletin 37(08):752. doi:10.1557/mrs.2012.174
6. Mie G (1908) Annalen der Physik 330(3):377. doi:10.1002/andp.19083300302
7. Taflove A, Hagness SC (2005) Computational electrodynamics: the finite-difference time-domain method, 3rd ed. Advanced Series in Applied Physics. Artech House
8. Waterman P (1965) Proc IEEE 53(8):805. doi:10.1109/PROC.1965.4058
9. Doicu A, Wriedt T, Eremin YA (2006) Light scattering by systems of particles. Springer Series in Optical Sciences, vol 124. Springer, Berlin. doi:10.1007/978-3-540-33697-6
10. Peterson B, Ström S (1973) Phys Rev D 8:3661. doi:10.1103/PhysRevD.8.3661
11. Xu Yl (1995) Appl Opt 34(21):4573. doi:10.1364/AO.34.004573
12. Xu Yl (1998) Applied Opt 37(27):6494. doi:10.1364/AO.37.006494
13. Draine BT, Flatau PJ (1994) J Opt Soc Am A 11(4):1491. doi:10.1364/JOSAA.11.001491
14. Hafner C (1990) The generalized multipole technique for computational electromagnetics. Artech House Books, Boston
15. García deAbajo FJ, Howie A (2002) Phys Rev B 65(11):115418. doi:10.1103/PhysRevB.65.115418
16. Busch K, König M, Niegemann J (2011) Laser Photonics Rev 5(6):773. doi:10.1002/lpor.201000045
17. Matyssek C, Niegemann J, Hergert W, Busch K (2011) Photonics Nanostruct Fundam Appl 9(4):367. doi:10.1016/j.photonics.2011.04.003
18. Geuquet N, Henrard L (2010) Ultramicroscopy 110(8):1075. doi:10.1016/j.ultramic.2010.01.013
19. Karamehmedović M, Schuh R, Schmidt V, Wriedt T, Matyssek C, Hergert W, Stalmashonak A, Seifert G, Stranik O (2011) Opt Express 19(9):8939. doi:10.1364/OE.19.008939

20. Ross MB, Schatz GC (2015) J Phys D Appl Phys 48(18):184004. doi:10.1088/0022-3727/48/18/184004
21. Ginzburg P, Berkovitch N, Nevet A, Shor I, Orenstein M (2011) Nano Lett 11(6):2329. doi:10.1021/nl200612f
22. Sukharev M, Seideman T (2006) J Chem Phys 124(14):144707. doi:10.1063/1.2177651
23. Sukharev M, Seideman T (2006) Nano Lett 6(4):715. doi:10.1021/nl0524896
24. Sukharev M, Seideman T (2007) J Phys B: At Mol Opt Phys 40(11):S283. doi:10.1088/0953-4075/40/11/S04
25. Forestiere C, Pasquale AJ, Capretti A, Miano G, Tamburrino A, Lee SY, Reinhard BM, Dal Negro L (2012) Nano Lett 12(4):2037. doi:10.1021/nl300140g
26. Barber PW, Hill SC (1990) Light scattering by particles: computational methods. Advanced Series in Applied Physics, vol 2. World Scientific
27. Mackowski DW (1991) Proc R Soc A: Math Phys Eng Sci 433(1889):599. doi:10.1098/rspa.1991.0066
28. Bohren CF, Huffman DR (2004) Absorption and scattering of light by small particles. Wiley-VCH
29. García de Abajo FJ (1999) Phys Rev B 59(4):3095. doi:10.1103/PhysRevB.59.3095
30. Thomas S (2013) Symmetrieeigenschaften und Optimierung photonischer und plasmonischer Nanostrukturen, Master thesis, Martin-Luther-Universität, Halle, Germany
31. Nelder JA, Mead R (1965) Comput J 7(4):308. doi:10.1093/comjnl/7.4.308
32. Höflich K, Becker M, Leuchs G, Christiansen S (2012) Nanotechnology, vol 23, p 185303, DOI doi:10.1088/0957-4484/23/18/185303
33. Chu W, Gao X, Sorooshian S (2011) Inf Sci 181(22):4909. doi:10.1016/j.ins.2011.06.024
34. Adcock S Genetic algorithm utility library, retrieved from http://gaul.sourceforge.net
35. Galassi M GNU scientific library reference manual, 3rd edn. ISBN 0954612078
36. Matyssek C, Schmidt V, Hergert W, Wriedt T (2012) Ultramicroscopy 117:46. doi:10.1016/j.ultramic.2012.04.002
37. Huang F, Baumberg JJ (2010) Nano Lett 10(5):1787. doi:10.1021/nl1004114
38. Vial A, Grimault AS, Macías D, Barchiesi D, de la Chapelle ML (2005) Phys Rev B 71(8):085416. doi:10.1103/PhysRevB.71.085416
39. Etchegoin PG, Le Ru EC, Meyer M (2006) J Chem Phys 125(16):164705. doi:10.1063/1.2360270
40. Matyssek CF (2012) Investigation of plasmonic structures by light and electron microscopy: contributions to an efficient numerical treatment. Dissertation, Martin-Luther-Universität, Halle, Germany
41. Johnson PB, Christy RW (1972) Phys Rev B 6(12):4370. doi:10.1103/PhysRevB.6.4370
42. Zeman EJ, Schatz GC (1987) J Phys Chem 91(3):634. doi:10.1021/j100287a028
43. Berciaud S, Cognet L, Tamarat P, Lounis B (2005) Nano Lett 5(3):515. doi:10.1021/nl050062t
44. Grady N, Halas N, Nordlander P (2004) Chem Phys Lett 399(1-3):167. doi:10.1016/j.cplett.2004.09.154
45. David C, de Abajo FJG (2011) J Phys Chem C 115(40):19470. doi:10.1021/jp204261u
46. de Abajo FJG (2008) J Phys Chem C 112(46):17983. doi:10.1021/jp807345h
47. Duan H, Fernández-Domínguez AI, Bosman M, Maier SA, Yang JKW (2012) Nano Lett 12(3):1683. doi:10.1021/nl3001309
48. Xu Yl, Khlebtsov NG (2003) J Quant Spectrosc Radiat Transf 79-80(0):1121. doi:10.1016/S0022-4073(02)00345-X
49. Yan B, Boriskina SV, Reinhard BM (2011) J Phys Chem C 115(11):4578. doi:10.1021/jp112146d
50. Zheng P, Cushing SK, Suri S, Wu N (2015) Phys Chem Chem Phys 17(33):21211. doi:10.1039/c4cp05291a